

Journal Pre-proof

Dynamic benzene adsorption performance of microporous TMA⁺-exchanged montmorillonite: The role of TMA⁺ cations

Liangliang Deng, Yaqi Liu, Guanzheng Zhuang, Peng Yuan, Dong Liu, Hongling Bu, Hongzhe Song, Li Li

PII: S1387-1811(19)30853-4

DOI: <https://doi.org/10.1016/j.micromeso.2019.109994>

Reference: MICMAT 109994

To appear in: *Microporous and Mesoporous Materials*

Received Date: 31 August 2019

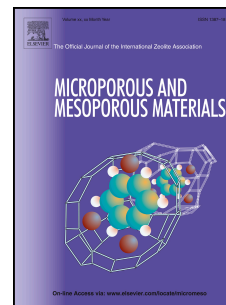
Revised Date: 19 December 2019

Accepted Date: 28 December 2019

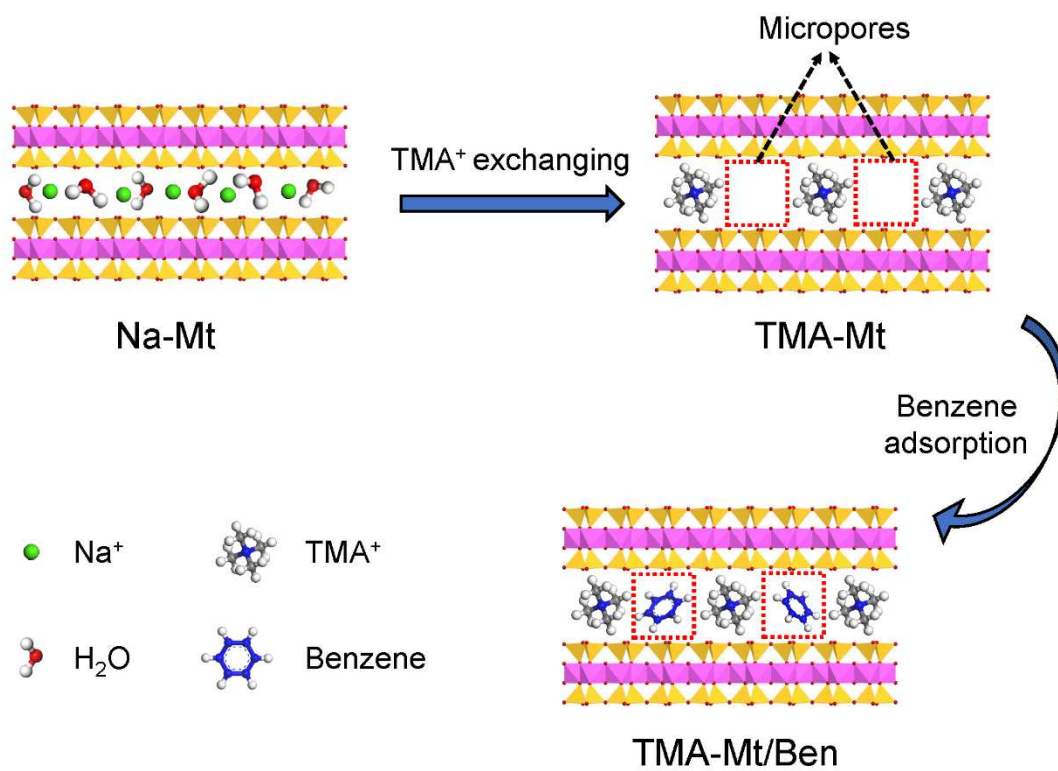
Please cite this article as: L. Deng, Y. Liu, G. Zhuang, P. Yuan, D. Liu, H. Bu, H. Song, L. Li, Dynamic benzene adsorption performance of microporous TMA⁺-exchanged montmorillonite: The role of TMA⁺ cations, *Microporous and Mesoporous Materials* (2020), doi: <https://doi.org/10.1016/j.micromeso.2019.109994>.

This is a PDF file of an article that has undergone enhancements after acceptance, such as the addition of a cover page and metadata, and formatting for readability, but it is not yet the definitive version of record. This version will undergo additional copyediting, typesetting and review before it is published in its final form, but we are providing this version to give early visibility of the article. Please note that, during the production process, errors may be discovered which could affect the content, and all legal disclaimers that apply to the journal pertain.

© 2019 Published by Elsevier Inc.



Graphical Abstract



17 **Abstract**

18 Tetramethylammonium (TMA^+) exchanged montmorillonites (TMA-Mts) of
19 various surfactant (TMA^+) dosages were prepared, and the roles of TMA^+ cations in
20 the microstructure and dynamic benzene adsorption performance of TMA-Mts were
21 investigated. TMA^+ cations were intercalated into the interlayer space of
22 montmorillonite (Mt), and they exhibited dual effects on the benzene adsorption by
23 TMA-Mts. For one thing, the intercalated TMA^+ cations arranged loosely, creating an
24 interlayer microporous structure. The interlayer micropores were important benzene
25 adsorption sites, and the dynamic benzene adsorption capacity (q value) positively
26 correlated to the microporous surface area (S_{micro}). The optimized dosage of TMA^+
27 was 1.5 times the cation exchange capacity of Mt itself, which resulted in a TMA-Mt
28 with the largest S_{micro} and q values of $65.0 \text{ m}^2/\text{g}$ and 425.3 mg/g , respectively. On the
29 other hand, the intercalated TMA^+ cations could interact with benzene molecules,
30 further increasing the benzene adsorption performance of TMA-Mt but decreasing the
31 diffusion and mass transfer of benzene molecules through TMA-Mt. In addition,
32 TMA-Mt displayed remarkable regenerability, with a recycling efficiency exceeding
33 90%. These results indicated that modifying montmorillonite with small quaternary
34 ammonium cation is an effective strategy to enhance the adsorption of volatile organic
35 compounds (VOCs) by Mt and the TMA-Mts are promising adsorbents for VOCs
36 remediation.

37 **Keywords:**38 Montmorillonite; TMA^+ exchanging; Surfactant dosage; Micropores; Dynamic

39 adsorption; Benzene

40 **1. Introduction**

41 Volatile organic compounds (VOCs), which emitted from the construction,
42 petrochemical, pharmaceutical, and printing industries, are the most common air
43 pollutants, and they are toxic and (in some cases) carcinogenic [1]. In addition, VOCs
44 are the primary contributors to photochemical pollution and secondary organic
45 aerosols, which are also harmful to human health [2-4]. Therefore, the treatment of
46 VOCs had received considerable attention. Many technologies have been developed
47 for VOCs control, such as membrane separation [5], oxidation [6], catalysis [7],
48 biological treatment [8], and adsorption [9], where adsorption is the most applicable
49 technology because of its low cost, low energy, and flexible system structure [10].

50 Adsorbents play an important role in the application of adsorption technology,
51 and activated carbon and synthetic zeolites are two types of commonly used VOCs
52 adsorbents. Activated carbon is inexpensive and exhibits excellent adsorption capacity
53 [11], but several drawbacks are associated with its use in the adsorption process, such
54 as fire risk, propensity for pore-clogging, and regeneration difficulties [12]. Synthetic
55 zeolites, such as ZSM-5 [13] and NaY zeolites [14], have the advantages in VOCs
56 adsorption due to their good chemical stability and controllable pore size, but their
57 wide application is restricted by their high cost. There is therefore an increasing focus
58 on the development of low-cost adsorbents with excellent adsorption performance and
59 desirable thermal stability. To this end, raw minerals have been proposed as possible
60 adsorbents due to their unique porous structure, excellent heat resistance, and low cost

61 [15].

62 Montmorillonite (Mt) is a 2:1 dioctahedral clay mineral comprising an octahedral
63 alumina sheet sandwiched between two opposing tetrahedral silica sheets, with
64 hydrated exchangeable cations incorporated within the interlayer space. In addition,
65 the substitution of Mg^{2+} or Fe^{2+} for Al^{3+} in octahedral sheets and substitution of Al^{3+}
66 for Si^{4+} in tetrahedral sheets often occurs in Mt, making the layers of Mt negatively
67 charged. Due to the exchangeable cations and negatively charged layers, Mt is widely
68 used as an efficient adsorbent for the removal of aqueous cationic pollutants, such as
69 dyes [16] and heavy metal ions [17], from wastewaters. However, the adsorption of
70 Mt for non-ionic organic pollutants (NOPs), e.g., benzene [18] and phenol [19], is
71 hindered by its hydrophilicity, which results from the exchangeable cations and
72 negatively charged layers. The modification of Mt via a cation-exchange reaction with
73 cationic surfactants, such as octadecyltrimethylammonium bromide (OTAB) [20],
74 cetyltrimethylammonium bromide (CTAB) [21], dodecyltrimethylammonium
75 bromide (DTAB) [22], and tetramethylammonium bromide (TMAB) [23], forms
76 organo-montmorillonites (OMts). The cationic surfactants are intercalated within the
77 interlayer spaces of Mt, leading to different overall physical and chemical properties
78 for OMts, including a NOPs absorptive capacity superior to that of Mt [24].

79 In physical terms, the intercalated surfactants convert the OMts surface from
80 hydrophilic to hydrophobic [25], and thus improve its affinity for hydrophobic NOPs.
81 Moreover, the intercalated surfactants affect the microstructure of OMts, resulting in
82 various NOPs adsorption behaviors. Two adsorption mechanisms have been reported:

83 (1) a partition process, and (2) a surface-adsorbent process [26, 27]. Previous studies
84 have revealed that the intercalation of large surfactants (e.g., CTAB and DTAB, as
85 mentioned above) in the interlayer space of Mt occurs via close packing to form
86 hydrophobic phase, which were considered to adsorb NOPs by a partition process [28].
87 Conversely, OMts modified with small surfactants (e.g., TMAB) usually adsorb
88 organic pollutants via a surface-adsorbent process, because small surfactant molecules
89 tend to be loosely arranged in the interlayer space, creating a number of micropores
90 [29].

91 Compared with the numerous studies of NOPs adsorption by OMts, the report on
92 the VOCs adsorption by OMts was rare, and the relevant mechanisms were still
93 unclear. Generally, an adsorbent with a large specific surface area (S_{BET}) and many
94 micropores will exhibit excellent VOCs adsorption performance [30]. The OMts
95 modified with small surfactants (e.g., TMAB) has a larger S_{BET} value and more
96 interlayer micropores than those OMts containing larger surfactants [29], and may
97 thus possess excellent VOCs adsorption performance. However, several factors, such
98 as surfactant size and charge density of Mt, influenced the microstructure of OMts
99 modified with small surfactants, and would thus have an impact on the VOCs
100 adsorption. Kukkadapu et al. [31] found that the organic-vapor adsorption
101 performance of OMts comprising small surfactants of different size (TMAB and
102 tetramethylphosphonium bromide) depended on their S_{BET} values, i.e., a larger value
103 of S_{BET} corresponded to a greater adsorption capability. Lee et al. [32] reported that
104 the charge density of Mt influenced the VOCs adsorption behavior of TMA-Mt by

105 affecting the packing density of TMA⁺ cations and the formation of micropores.

106 However, the adsorption behavior of OMts incorporating small surfactants is not
107 only regulated by surfactant size and charge density of Mt, but also affected by
108 surfactant dosage, which controls the microstructure of the resulting OMts [29].
109 Surprisingly, the role of TMA⁺ cations on the VOCs adsorption performance of
110 TMA-Mts with different TMA⁺ dosages has not been reported.

111 In addition, in previous research, VOCs adsorption by TMA-Mts was evaluated
112 using static adsorption experiment [31, 32], whose processes include the
113 pre-evacuating of adsorbents and the altering of adsorption and desorption
114 equilibrium pressures [33]. In comparison, dynamic adsorption experiment conducted
115 at room temperature and atmospheric pressure can be used to simulate the real
116 adsorption behavior of adsorbents for industrial VOCs-absorbing applications. Hence,
117 studying the dynamic adsorption of VOCs by TMA-Mts is necessary for further
118 applications of this technique.

119 To examine these two areas, the microstructure of TMA-Mts prepared with
120 various TMA⁺ dosages were characterized. Benzene, one of the most common VOCs
121 pollutants, was used to investigate the dynamic adsorption behavior of TMA-Mts.
122 Finally, the role of TMA⁺ cations on the dynamic benzene adsorption performance of
123 TMA-Mts was examined and discussed.

124

125 **2. Experiment**

126 **2.1 Materials**

127 Mt sourced from Inner Mongolia, China, was purified by a conventional
128 sedimentation method, and its chemical composition was as follows: SiO₂, 57.41%;
129 Al₂O₃, 15.66%; Fe₂O₃, 4.93%; MgO, 4.98%; K₂O, 0.12%; CaO, 2.98%; Na₂O, 0.11%;
130 MnO, 0.03%; TiO₂, 0.31%; and ignition loss, 13.33%. The cation-exchange capacity
131 (CEC) of purified Mt, measured by adsorption of [Co(NH₃)₆]³⁺ [34], was 110.5
132 meq/100g. TMAB (> 98%) was purchased from Sigma-Aldrich Chemistry Co., Ltd.

133 2.2 Preparation of TMA-Mt

134 Sodium-based montmorillonite (Na-Mt) was firstly prepared as follows: 10.0 g
135 purified Mt was dispersed in 200 mL of a 0.5 M sodium chloride solution under
136 vigorous stirring at 80°C for 24 h. After this time, the solid phase was then separated
137 from the solution by centrifugation and then re-treated with 200 mL of 0.5 M sodium
138 chloride solution, and the resulting mixture was heated and then separated as before.
139 This procedure was repeated once more to effect complete cation exchange. The
140 Na-Mt product was repeatedly washed with distilled water and then dried at 60°C
141 overnight before it was ground to a powder.

142 TMA-Mt was prepared by the following method: a desired amount of TMAB,
143 equating to several times (0.25, 0.5, 1.0, 1.5, and 2.0, respectively) of the CEC of the
144 amount of Na-Mt, was dispersed in 200 mL of distilled water, and the solution was
145 stirred at 80°C for 30 min. Then, 10.0 g Na-Mt was added slowly into the solution,
146 and the mixture was stirred at 60°C for 12 h. After this time, the solids were separated
147 by filtration, repeatedly washed with distilled water to remove excess TMAB, and
148 then dried and ground. The products are denoted as TMA-Mtx, where x was the

149 dosage of TMAB. For example, TMA-Mt_{0.25} denotes TMA-Mt with a TMAB dosage
150 of 0.25 CEC.

151

152 **2.3 Characterization methods**

153 Major element oxides were analyzed on fused glass beads with a Rigaku RIX
154 2000 X-ray fluorescence spectrometer. To determine loss on ignition, 1000 mg of
155 sample powder was heated to 1000°C and maintained there for 10 min.

156 The CHN elemental analysis was performed using an ElementarVario EL III
157 Universal CHNOS Elemental Analyzer.

158 The thermogravimetric (TG) analysis was conducted on a Netzsch STA 409PC
159 instrument. Approximately 10 mg of the sample was heated in a corundum crucible
160 from 30 to 1000 °C at a heating rate of 10 °C/min under a highly pure N₂ atmosphere
161 (20 cm³/min).

162 The X-ray diffraction (XRD) patterns were recorded with a Bruker D8 Advance
163 diffractometer with a Ni filter and Cu-K α radiation ($\lambda = 0.154$ nm) using a generator
164 voltage of 40 kV and a current of 40 mA. The scan rate was 3° (2 θ)/min.

165 Ar adsorption-desorption isotherms were measured with a Micromeritics
166 ASAP-2460 Accelerated Surface Area and Porosimetry system at liquid-argon
167 temperature. The samples were outgassed at 120°C for 12 h before measurements
168 were made. The samples' S_{BET} values were calculated from the argon adsorption data
169 using the multiple-point Brunauer-Emmett-Teller (BET) method [35], and the total
170 pore volume (V_{total}) was estimated based on the argon uptake at a relative pressure of

171 approximately 0.98. The samples' microporous surface area (S_{micro}) and microporous
172 volume (V_{micro}) were derived using the t -plot method [36]. The non-local density
173 functional theory (NLDFT) model [37] was used to determine the samples' micropore
174 size distributions.

175 Diffuse reflectance infrared Fourier-transform (DRIFT) characterization was
176 performed on the Praying Mantis™ diffuse reflection accessory (Harrick Scientific
177 Products INC) of a Bruker Vertex-70 Fourier transform infrared spectrometer at room
178 temperature. The DRIFT measurement lasted for 2 min (from the sample loading to
179 the spectrum recording), and the ambient relative humidity was approximately 30%.
180 The spectra were collected over the range of 600–4000 cm^{-1} with 64 scans and a
181 resolution of 4 cm^{-1} using a KBr background.

182 **2.4 Benzene adsorption test**

183 The samples' benzene adsorption performance was evaluated with an in-line gas
184 chromatography apparatus (Fig. 1). Before adsorption, the samples were heated at
185 120°C in a muffle oven for 2 h to remove most of the physically adsorbed water
186 molecules and small organic impurities adsorbed in the pores. During the adsorption
187 measurement, an organic saturator containing 200 mL benzene was immersed in a
188 water bath at 30°C. Each powder sample was weighed accurately to 0.5 g and loaded
189 into a glass column. The column was fed with a dry nitrogen stream containing
190 benzene vapor at 3.00 mL/min, which was adjusted as required with a mass flow
191 controller (MFC). The concentrations of benzene in both the column influent and
192 effluent were quantified with a gas chromatograph (Agilent 7820A) using flame

193 ionization detection. The experiment stopped when the adsorption equilibrium for the
 194 adsorbent was reached. After adsorption, the glass column containing the sample was
 195 heated at 120°C for 12 h for desorption of the adsorbed benzene molecules, cooled to
 196 room temperature, and retested. This adsorption-desorption cycle test was performed
 197 four times to evaluate the samples' regenerative and re-use performance.

198 The adsorbents' benzene adsorption capacity (q , mg/g) was calculated by
 199 integrating the area above the acquired breakthrough curve after subtracting the area
 200 attributable to dead volume in the system, according to the following equation:

$$201 \quad q = \frac{M}{1000m} \int_{t_1}^{t_2} F[C_0 - C_t] dt \quad \text{Eq. (1)}$$

202 where M (g/mol) is the molecular mass of benzene; m (g) is the initial mass of
 203 the adsorbents before testing; t_1 (min) is the breakthrough time without the samples; t_2
 204 (min) is the breakthrough time with the packed column; C_0 and C_t (mmol/L) represent
 205 the influent and measured effluent benzene concentrations, respectively; and F
 206 (mL/min) is the N₂ flow rate. The dead volume was determined by performing blank
 207 runs without the column.

208 The breakthrough curves were fitted using the Yoon and Nelson model [38], as
 209 per Eq (2):

$$210 \quad t = \tau + \frac{1}{k} \ln \frac{C_t}{C_0 - C_t} \quad \text{Eq. (2)}$$

211 where t (min) is the breakthrough time; C_t and C_0 are the outlet and inlet
 212 concentrations of the stream through the adsorbent column, respectively; τ (min) is the
 213 time at which the breakthrough concentration reached half the initial concentration (C_t
 214 = 0.5 C_0); and k is the mass transfer coefficient.

215

216

217

218 3. Results and discussion

219 3.1 Microstructure of TMA-Mtx samples

220 The XRD patterns of Na-Mt and TMA-Mtx samples are presented in Fig. 2. The
221 (001) reflection of Na-Mt occurs at 7.2° (2θ), corresponding to a d_{001} -value of 1.26
222 nm. A weak reflection at 27° is attributed to quartz (ca. wt. 3%). Compared to Na-Mt,
223 the d_{001} -values of TMA-Mtx samples increased to 1.31 nm (TMA-Mt_{0.25}) and 1.38 nm
224 (TMA-Mt_{0.5}, TMA-Mt_{1.0}, TMA-Mt_{1.5}, and TMA-Mt_{2.0}), corresponding to interlayer
225 distances of 0.35 nm and 0.42 nm. These were calculated by subtracting the thickness
226 of the structural TOT layer unit (0.96 nm) from d_{001} -value. The increase of the basal
227 spacing demonstrates the successful intercalation of TMA⁺ cations, in accordance
228 with previous study [23]. The basal spacing of TMA-Mtx samples was positively
229 influenced by surfactant (TMA⁺) dosage. However, TMA⁺ dosage of more than 0.5
230 CEC resulted in the same basal spacing. This phenomenon indicates that the basal
231 spacing of TMA-Mtx samples is limited.

232 The carbon (f_C) and nitrogen (f_N) content of Na-Mt and TMA-Mtx samples are
233 listed in Table 1. The f_C and f_N of TMA-Mtx samples were larger than those of Na-Mt
234 and enlarged with the increase of TMA⁺ dosage. These results were ascribed to the
235 increase in the amount of intercalated TMA⁺ cations. The Δf_C and Δf_N values (Table 1)
236 dramatically increased until the TMA⁺ dosage reached 1.0 CEC while more TMA⁺

237 resulted in only a little increase of Δf_C and Δf_N values. This phenomenon suggests that
238 the TMA^+ dosage of 1.0 CEC is a critical point which indicates different intercalation
239 mechanisms [39]. TMA^+ cations intercalated into the interlayer space of Na-Mt
240 mainly by ion-exchanging when TMA^+ dosage is less than 1.0 CEC, while TMA^+
241 cations can be also physically adsorbed into the interlayer space and/or surface of
242 Na-Mt via ion pairs when they are more than 1.0 CEC. However, only a few TMA^+
243 cations can occupy the interlayer space and surface by physical adsorption.

244 TG/DTG measurement was performed to calculate the content of TMA^+ in
245 TMA-Mtx samples. The TG curve of Na-Mt (Fig. 3a) showed two mass loss steps in
246 the temperature range of 30-200°C and 500-700°C with the related DTG peaks
247 centered at 115.7 and 626.6°C, respectively. The former substantial loss was attributed
248 to the dehydration of adsorbed water and interlayer water, indicating a water content
249 of 10.03%. While, the latter mass loss occurred at a temperature of higher than 500°C
250 was caused by the dehydroxylation of Na-Mt [40]. Three major mass loss steps
251 centered at 113.2, 397.5, and 585.7°C are resolved in the TG curve of TMA-Mt_{0.25}
252 (Fig. 3b): (1) the removal of adsorbed water and interlayer water at 30-200°C, (2) the
253 decomposition of the intercalated TMA^+ in the temperature range of 200-500°C, and
254 (3) the dehydroxylation at the temperature above 500°C. Compared to Na-Mt, the
255 water content of TMA-Mt_{0.25} decreased to 9.13%. This result was due to improvement
256 of the hydrophobicity of Na-Mt by the intercalation of TMA^+ cations with a content of
257 4.22%. With the increase of the TMA^+ dosage, the water content of TMA-Mt_{0.5},
258 TMA-Mt_{1.0}, TMA-Mt_{1.5}, and TMA-Mt_{2.0} (Fig. 3c-f) further decreased to 8.43%,

259 7.36%, 6.59%, and 5.80%, respectively, but their content of intercalated TMA⁺
260 cations increased to 5.83%, 8.68%, 9.52%, and 10.11%, respectively. These results
261 confirmed the enhancement of hydrophobicity of TMA-Mtx samples by the
262 intercalation of TMA⁺ cations.

263 The Ar adsorption-desorption isotherms of Na-Mt and TMA-Mtx samples are
264 displayed in Fig. 4a. According to the IUPAC classification refined by Thommes et al.
265 [37], the isotherm of Na-Mt was classified as type II with an H3 hysteresis loop,
266 which is a characteristic of plate materials with non-rigid slit-like pores [41].
267 Hysteresis is associated with the filling and emptying of mesopores via capillary
268 condensation, where these mesopores result from the disordered stacking of Na-Mt
269 particles. A slightly steeper increase in adsorption at a low relative pressure ($P/P_0 <$
270 0.1) in the isotherm of Na-Mt (Fig. 4a) indicated the presence of micropores in this
271 substrate. These micropores corresponded to the slit-shaped micropores created by the
272 turbostratic stacking of clay particles and/or the interlayer micropores resulting from
273 dehydration [15].

274 The isotherms of TMA-Mtx samples (Fig. 4a) present mixed characteristics of
275 type I(a) and IV(a) with an H3 hysteresis loop, which indicated the coexistence of
276 microporosity and mesoporosity. The hysteresis loop was caused by mesopores
277 formed by disordered stacking of particles. Moreover, the amount of adsorbed Ar at
278 relatively low pressure ($P/P_0 < 0.1$) in the isotherms of TMA-Mtx samples increased
279 much more rapidly than that amount adsorbed in Na-Mt, suggesting that TMA-Mtx
280 samples had a more highly developed microporosity than Na-Mt. This can be

281 attributed to the intercalated TMA⁺ cations, which created a number of micropores in
282 the interlayer of TMA-Mtx samples.

283 The micropore size distribution (PSD) curves of Na-Mt and TMA-Mtx samples
284 (Fig. 4b) showed a minor distribution at 1.17 nm, which is much greater than the
285 interlayer distance of Na-Mt and TMA-Mx samples. Hence, these micropores
286 probably resulted from the turbostratic stacking of particle. In addition, a remarkable
287 distribution centered at 0.51 nm appeared in the PSD curves of TMA-Mt_{0.25}. With the
288 increase of TMA⁺ dosage, the diameters of these micropores decreased in TMA-Mt_{0.5}
289 (0.48 nm) and TMA-Mt_{1.0} (0.47 nm), and finally decreased to lower than the detection
290 limit in TMA-Mt_{1.5} and TMA-Mt_{2.0}. Hence, these micropores were attributed to the
291 unevenly occupation of TMA⁺ cations in the interlayer space. The increase of the
292 density of intercalated TMA⁺ cations leads to close packing from loose distribution,
293 resulting in the decrease of micropore size.

294 The porous parameters of the Na-Mt and TMA-Mtx samples are listed in Table 2.
295 Na-Mt showed the smallest S_{BET} (55.9 m²/g) due to its poorest microporosity, of which
296 the S_{micro} was only 3.3 m²/g. This result was in accordance with the slight phenomenon
297 of micropore filling in the Ar adsorption-desorption isotherms of Na-Mt (Fig. 4a).
298 After TMA⁺ exchanging, the S_{BET} and S_{micro} of TMA-Mtx samples increased, owing to
299 the formation of the interlayer micropores by the intercalation of TMA⁺ cations.
300 TMA-Mt_{1.5} had the highest S_{BET} and S_{micro} (173.5 m²/g and 65.0 m²/g, respectively),
301 indicating that a dosage of 1.5 CEC is considered the critical point. When the TMA⁺
302 dosage outstripped 1.5 CEC, the exceeded TMA⁺ cations could also be intercalated

303 into the interlayer space of Na-Mt by adsorption, resulting in the decrease of the
304 interlayer microporosity of TMA-Mtx samples.

305 **3.2 Dynamic benzene adsorption of TMA-Mtx samples**

306 The breakthrough curves of Na-Mt and TMA-Mtx samples (Fig. 5) were used to
307 evaluate their dynamic adsorption capacity (q value, Table 3). Na-Mt had the lowest q
308 value (87.1 mg/g), attributing to its smallest S_{BET} and least amount of micropores. In
309 addition, as the XRD patterns (Fig. 2) indicated, the interlayer distance of Na-Mt was
310 only approximately 0.30 nm, which was less than the van der Waals diameter of the
311 carbon atom (0.34 nm), the smallest one-dimensional size that a benzene molecule
312 could adopt. Therefore, only a small number of the interlayer micropores of Na-Mt
313 (i.e. the micropores with the pore width larger than 0.34 nm) were available for
314 benzene adsorption. Compared to Na-Mt, the q values of TMA-Mtx samples (Table 3)
315 increased, indicating that the intercalation of TMA⁺ cations enhanced the adsorption
316 of benzene by Mt, which could be ascribed to the introduced micropores by the
317 intercalated TMA⁺ cations.

318 The interlayer distance of TMA-Mt_{0.25} reached 0.35 nm, which was greater than
319 the van der Waals diameter of the carbon atom (0.34 nm). As a result, a considerable
320 number of benzene molecules could be adsorbed into the interlayer micropores of
321 TMA-Mt_{0.25}, resulting in the higher q value of TMA-Mt_{0.25} (184.3 mg/g) compared to
322 that of Na-Mt (87.1 mg/g). When the dosage exceeded 0.25 CEC, the interlayer
323 distance of TMA-Mtx samples increased to 0.41 nm, thus more micropores, which
324 were available for benzene adsorption, were generated by the intercalated TMA⁺

325 cations, leading to a further improvement in the benzene adsorption performance of
326 the TMA-Mtx samples. The q value of TMA-Mt_{1.5} (425.3 mg/g) was the highest
327 among the TMA-Mtx samples because it had the largest S_{micro} (65.0 m²/g). This result
328 suggested that the q values of the TMA-Mtx samples correlated to their S_{micro} ,
329 confirming the significant impact of micropores on the benzene adsorption
330 performance of TMA-Mtx samples. However, TMA-Mt_{2.0} had a higher q value (419.0
331 mg/g) than TMA-Mt_{0.5} (220.9 mg/g) and TMA-Mt_{1.0} (380.8 mg/g), even though its
332 S_{micro} (55.9 m²/g) was smaller than those of TMA-Mt_{0.5} (59.9 m²/g) and TMA-Mt_{1.0}
333 (61.8 m²/g). This fact indicated that interlayer micropores were not the only factor
334 affecting the benzene adsorption performance of the TMA-Mtx samples. The superior
335 benzene adsorption performance of TMA-Mt_{2.0} towards TMA-Mt_{0.5} and TMA-Mt_{1.0}
336 might be due to its larger content of TMA⁺ cations (10.11%) than TMA-Mt_{0.5} (5.83%)
337 and TMA-Mt_{1.0} (8.68%), as the TG curves (Fig. 3c, 3d, and 3f) revealed. More
338 intercalated TMA⁺ cations resulted in better hydrophobicity of the TMA-Mtx samples,
339 improving the compatibility between TMA-Mtx and benzene molecules.

340 The k values of the Na-Mt and TMA-Mtx samples, which represent the diffusion
341 and mass transfer characteristics of benzene molecules in the adsorption process, are
342 listed in Table 3. Generally, a small k value indicates that the adsorbate has minimal
343 diffusion and mass transfer ability. Thus, the smaller k values of TMA-Mtx samples
344 compared with that of Na-Mt indicated that there was lower propensity for diffusion
345 and mass transfer of benzene molecules in TMA-Mtx samples than in Na-Mt. This
346 may be attributable to the adsorption by the interlayer micropores introduced by

347 intercalated TMA⁺ cations. However, TMA-Mt_{1.5} had a slightly larger *k* value (0.059)
348 than TMA-Mt_{2.0} (0.058) even though it possessed the highest S_{micro} value (65.0 m²/g),
349 indicating that the diffusion and mass transfer of benzene molecules occurred more
350 easily in TMA-Mt_{1.5} than in TMA-Mt_{2.0}. This result further confirmed that other
351 factors aside from micropores affected the benzene adsorption of TMA-Mtx samples,
352 which might be ascribed to the interaction between the intercalated TMA⁺ cations and
353 benzene molecules.

354 To detect the interaction between the benzene molecules and TMA-Mtx samples,
355 DRIFT characterization was performed on benzene and TMA-Mt_{1.5} before and after
356 benzene adsorption. The sample obtained after TMA-Mt_{1.5} adsorbed benzene was
357 denoted TMA-Mt_{1.5}/Ben. The DRIFT spectra of benzene, TMA-Mt_{1.5}, and
358 TMA-Mt_{1.5}/Ben are displayed in Fig. 6. After benzene adsorption, four bands at 3035,
359 3060, 3069, and 3090 cm⁻¹ appeared in the DRIFT spectrum of TMA-Mt_{1.5}/Ben.
360 These bands were due to the C–H stretching of aromatic rings [42-44], indicating that
361 benzene molecules were adsorbed in TMA-Mt_{1.5}. In addition, these bands shifted
362 slightly compared with those of benzene, which could be due to the interaction
363 between adsorbed benzene molecules and intercalated TMA⁺ cations. Therefore, the
364 intercalated TMA⁺ cations were also the adsorption sites for benzene molecules in
365 addition to their introduced micropores.

366 Evaluation of the regeneration performance of VOCs adsorbents is an important
367 factor for determining their industrial potential [45]. Accordingly, the breakthrough
368 process of benzene adsorption on TMA-Mt_{1.5} was performed four times (Fig. 7). The

369 overlapping breakthrough curves of TMA-Mt_{1.5} exhibited that there was good
370 reusability of TMA-Mt_{1.5} over four cycles of benzene adsorption. In addition, the
371 recycling efficiency of TMA-Mt_{1.5} after four cycles of benzene adsorption still
372 exceeded 90% (Table 4), indicating the excellent regenerative performance of this
373 material.

374 Raw minerals are potential adsorbents for VOCs treatment. Previous studies [15,
375 46] had investigated the dynamic benzene adsorption performance of various minerals,
376 including diatomite (Dt), kaolinite (Kaol), halloysite (Hal), calcium-based
377 montmorillonite (Ca-Mt), and allophane (Allo). However, the microstructures and
378 surface properties of these minerals were different with those of TMA-Mt_{1.5}, leading
379 to their lower q values.

380 The benzene adsorption on Dt, Kaol, and Hal mainly occurred at their surface
381 due to the absence of appropriately sized micropores. However, their S_{BET} were
382 relatively small, which were 17.9, 17.9, and 58.4 m²/g, respectively, indicating the
383 relatively small amount of surface sites for adsorption. In addition, the surfaces of Dt,
384 Kaol, and Hal were significantly hydroxylated (and thus hydrophilic) that they were
385 less favorable for benzene adsorption. Therefore, the q values of Dt, Kaol, and Hal,
386 which were 74.5, 56.7, and 68.1 mg/g, respectively, were lower than that of
387 TMA-Mt_{1.5} (425.3 mg/g).

388 The interlayer distance of Ca-Mt (0.58 nm) was larger than that of TMA-Mt_{1.5}
389 (0.42 nm), and it was also close to the kinetic diameter of the benzene molecule (0.59
390 nm). Therefore, the interlayer space of Ca-Mt could theoretically accommodate

391 benzene adsorption. However, the interlayer space of Ca-Mt was generally occupied
392 by interlayer water, which would hinder the benzene adsorption. Therefore, the q
393 value of Ca-Mt (141.2 mg/g) was still lower than that of TMA-Mt_{1.5} (425.3 mg/g).

394 Allo possessed a substantial quantity of micropores, of which the S_{micro} reached
395 183.8 m²/g. However, the Allo nanoparticles aggregated extensively, resulting in the
396 formation of numerous pores with irregular channels, which are difficult for benzene
397 molecules to penetrate. Moreover, numerous hydroxyl groups were found to be
398 distributed on the surface of Allo. Therefore, the q value of Allo (105.9 mg/g) was
399 lower than that of TMA-Mt_{1.5} (425.3 mg/g).

400 Compared to activated carbon, which is flammable and generally requires high
401 temperature steam and/or nitrogen (>120°C) for its regeneration [47, 48], TMA-Mt_{1.5}
402 can be regenerated by heating at a relatively low temperature of 120°C after benzene
403 adsorption. Moreover, TMA-Mt_{1.5} has a high recycling efficiency (exceeded 90%)
404 after four cycles of benzene adsorption. Therefore, TMA-Mt_{1.5} appears to have a
405 greater thermal regeneration advantage than activated carbon.

406 **4. Conclusion**

407 In this study, the roles of TMA⁺ cations in the microstructure and dynamic
408 benzene adsorption performance of TMA-Mts with various TMA⁺ dosages were
409 investigated. TMA⁺ was intercalated into the interlayer space of Mt, with the numbers
410 of micropores generated depending on the dosage of TMA⁺.

411 The microporous surface area increased with the increase of TMA⁺ dosage, and
412 achieved a maximum at 1.5 CEC. The addition of more TMA⁺ cations (e.g., > 2.0

413 CEC) led to a decline of microporous surface area due to the closer packing of TMA⁺
414 cations. The dynamic benzene adsorption capacity of TMA-Mts was positively
415 influenced by their microporous surface area.

416 In addition to micropores, the intercalated TMA⁺ cations were another site for
417 benzene adsorption, enhancing the benzene adsorption performance of TMA-Mts but
418 decreasing the diffusion and mass transfer of benzene molecules through TMA-Mts. It
419 has thus been shown that TMA-Mt may be utilized as an effective VOCs adsorbent
420 due to its excellent dynamic benzene adsorption performance and superior
421 regenerability.

422

423 **Acknowledgements**

424 Financial supports from the Science and Technology Planning Project of
425 Guangdong Province, China (Grant No. 2017B020237003) and National Natural
426 Science Foundation of China (Grant No. 41672042) and Youth Innovation Promotion
427 Association of CAS for the excellent members (2016-81-01) and Natural Science
428 Foundation for Distinguished Young Scientists of Guangdong Province (Grant No.
429 2016A030306034) and the Youth Top-notch Talent Special Support Program of
430 Guangdong (Grant No. 609254605090) are gratefully acknowledged. This is a
431 contribution from GIGCAS.

432

433 **References**

434 [1] P. Wang, W. Zhao, Assessment of ambient volatile organic compounds (VOCs) near major

- 435 roads in urban Nanjing, China, *Atmos. Res.* 89 (2008) 289-297.
- 436 [2] Z.H. Ling, H. Guo, Contribution of VOC sources to photochemical ozone formation and its
437 control policy implication in Hong Kong, *Environ. Sci. Policy*, 38 (2014) 180-191.
- 438 [3] M. Claeys, W. Wang, A.C. Ion, I. Kourtchev, A. Gelencsér, W. Maenhaut, Formation of
439 secondary organic aerosols from isoprene and its gas-phase oxidation products through
440 reaction with hydrogen peroxide, *Atmos. Environ.* 38 (2004) 4093-4098.
- 441 [4] D. Melanie, K.G. Sexton, J. Harvey, B. Kevin, J. Ilona, Effects of 1,3-butadiene, isoprene, and
442 their photochemical degradation products on human lung cells, *Environ. Health Persp.* 112
443 (2004) 1488-1495.
- 444 [5] Y. Liu, X. Feng, D. Lawless, Separation of gasoline vapor from nitrogen by hollow fiber
445 composite membranes for VOC emission control, *J. Membrane Sci.* 271 (2006) 114-124.
- 446 [6] J. Luo, Q. Zhang, A. Huang, S.L. Suib, Total oxidation of volatile organic compounds with
447 hydrophobic cryptomelane-type octahedral molecular sieves, *Micropor. Mesopor. Mat.* 35
448 (2000) 209-217.
- 449 [7] S. Zuo, R. Zhou, Influence of synthesis condition on pore structure of Al pillared clays and
450 supported Pd catalysts for deep oxidation of benzene, *Micropor. Mesopor. Mat.* 113 (2008)
451 472-480.
- 452 [8] B. Guieysse, C. Hort, V. Platel, R. Munoz, M. Ondarts, S. Revah, Biological treatment of
453 indoor air for VOC removal: Potential and challenges, *Biotechnol. Adv.* 26 (2008) 398-410.
- 454 [9] W. Yuan, Y. Peng, L. Dong, W. Yu, L. Deng, F. Chen, Novel hierarchically porous
455 nanocomposites of diatomite-based ceramic monoliths coated with silicalite-1 nanoparticles
456 for benzene adsorption, *Micropor. Mesopor. Mat.* 206 (2015) 184-193.

- 457 [10] W. Yu, L. Deng, P. Yuan, D. Liu, W. Yuan, F. Chen, Preparation of hierarchically porous
458 diatomite/MFI-type zeolite composites and their performance for benzene adsorption: The
459 effects of desilication, *Chem. Eng. J.* 270 (2015) 450-458.
- 460 [11] D. Liu, P. Yuan, D. Tan, H. Liu, T. Wang, M. Fan, J. Zhu, H. He, Facile preparation of
461 hierarchically porous carbon using diatomite as both template and catalyst and methylene
462 blue adsorption of carbon products, *J. Colloid Interface Sci.* 388 (2012) 176-184.
- 463 [12] Z. Li, Y. Liu, X. Yang, Y. Xing, Q. Yang, R.T. Yang, Adsorption thermodynamics and
464 desorption properties of gaseous polycyclic aromatic hydrocarbons on mesoporous
465 adsorbents, *Adsorption* 23 (2017) 361-371.
- 466 [13] W. Song, R. Justice, C. Jones, V. Grassian, S. Larsen, Synthesis, characterization, and
467 adsorption properties of nanocrystalline ZSM-5, *Langmuir* 20 (2004) 8301-8306.
- 468 [14] J. Pires, A. Carvalho, M.B. de Carvalho, Adsorption of volatile organic compounds in Y
469 zeolites and pillared clays, *Micropor. Mesopor. Mat.* 43 (2001) 277-287.
- 470 [15] L. Deng, P. Yuan, D. Liu, F. Annabi-Bergaya, J. Zhou, F. Chen, Z. Liu, Effects of
471 microstructure of clay minerals, montmorillonite, kaolinite and halloysite, on their benzene
472 adsorption behaviors, *Appl. Clay Sci.* 143 (2017) 184-191.
- 473 [16] C. Almeida, N. Debacher, A. Downs, L. Cottet, C. Mello, Removal of methylene blue from
474 colored effluents by adsorption on montmorillonite clay, *J. Colloid Interface Sci.* 332 (2009)
475 46-53.
- 476 [17] O. Abollino, M. Aceto, M. Malandrino, C. Sarzanini, E. Mentasti, Adsorption of heavy metals
477 on Na-montmorillonite. Effect of pH and organic substances, *Water Res.* 37 (2003)
478 1619-1627.

- 479 [18] X. Liu, R. Zhu, J. Ma, F. Ge, Y. Xu, Y. Liu, Molecular dynamics simulation study of benzene
480 adsorption to montmorillonite: Influence of the hydration status, *Colloid Surf. A* 434 (2013)
481 200-206.
- 482 [19] L. Ma, Q. Chen, J. Zhu, Y. Xi, H. He, R. Zhu, Q. Tao, G.A. Ayoko, Adsorption of phenol and
483 Cu (II) onto cationic and zwitterionic surfactant modified montmorillonite in single and
484 binary systems, *Chem. Eng. J.* 283 (2016) 880-888.
- 485 [20] Y. Xi, Q. Zhou, R.L. Frost, H. He, Thermal stability of octadecyltrimethylammonium
486 bromide modified montmorillonite organoclay, *J. Colloid Interface Sci.* 311 (2007) 347-353.
- 487 [21] B. Hu, H. Luo, Adsorption of hexavalent chromium onto montmorillonite modified with
488 hydroxyaluminum and cetyltrimethylammonium bromide, *Appl. Surf. Sci.* 257 (2010)
489 769-775.
- 490 [22] J. Pan, G. Yang, B. Han, H. Yan, Studies on interaction of dodecyltrimethylammonium
491 bromide with Na- and Al-montmorillonite, *J. Colloid Interface Sci.* 194 (1997) 276-280.
- 492 [23] J.J. Stevens, S.J. Anderson, S.A. Boyd, FTIR study of competitive water-arene sorption on
493 tetramethylammonium- and trimethylphenylammonium-montmorillonites, *Clay Clay Miner.*
494 44 (1996) 88-95.
- 495 [24] N. Liu, M.-x. Wang, M.-m. Liu, F. Liu, L. Weng, L.K. Koopal, W.-f. Tan, Sorption of
496 tetracycline on organo-montmorillonites, *J. Hazard. Mater.* 225 (2012) 28-35.
- 497 [25] Y. Park, Z. Sun, G.A. Ayoko, R.L. Frost, Bisphenol A sorption by organo-montmorillonite:
498 Implications for the removal of organic contaminants from water, *Chemosphere* 107 (2014)
499 249-256.
- 500 [26] H. Zhao, G.F. Vance, Sorption of trichloroethylene by organo-clays in the presence of humic

- 501 substances, *Water Res.* 32 (1998) 3710-3716.
- 502 [27] S. Lin, M. Cheng, Adsorption of phenol and m-chlorophenol on organobentonites and
503 repeated thermal regeneration, *Waste Manage.* 22 (2002) 595-603.
- 504 [28] L. Zhu, B. Chen, X. Shen, Sorption of phenol, p-nitrophenol, and aniline to dual-cation
505 organobentonites from water, *Environ. Sci. Technol.* 34 (2000) 468-475.
- 506 [29] C.-C. Wang, L.-C. Juang, C.-K. Lee, T.-C. Hsu, J.-F. Lee, H.-P. Chao, Effects of exchanged
507 surfactant cations on the pore structure and adsorption characteristics of montmorillonite, *J.*
508 *Colloid Interface Sci.* 280 (2004) 27-35.
- 509 [30] C. Long, Y. Li, W. Yu, A. Li, Removal of benzene and methyl ethyl ketone vapor:
510 Comparison of hypercrosslinked polymeric adsorbent with activated carbon, *J. Hazard. Mater.*
511 203 (2012) 251-256.
- 512 [31] R.K. Kukkadapu, S.A. Boyd, Tetramethylphosphonium-and tetramethylammonium-smectites
513 as adsorbents of aromatic and chlorinated hydrocarbons: Effect of water on adsorption
514 efficiency, *Clay Clay Miner.* 43 (1995) 318-323.
- 515 [32] J.-F. Lee, M.M. Mortland, C.T. Chiou, D.E. Kile, S.A. Boyd, Adsorption of benzene, toluene,
516 and xylene by two tetramethylammonium-smectites having different charge densities, *Clay*
517 *Clay Miner.* 38 (1990) 113-120.
- 518 [33] G. Wang, B. Dou, Z. Zhang, J. Wang, H. Liu, Z. Hao, Adsorption of benzene, cyclohexane
519 and hexane on ordered mesoporous carbon, *J. Environ. Sci.* 30 (2015) 65-73.
- 520 [34] L. Zhu, R. Zhu, L. Xu, X. Ruan, Influence of clay charge densities and surfactant loading
521 amount on the microstructure of CTMA–montmorillonite hybrids, *Colloid Surf. A* 304 (2007)
522 41-48.

- 523 [35] S. Brunauer, P.H. Emmett, E. Teller, Adsorption of gases in multimolecular layers, *J. Am.*
524 *Chem. Soc.* 60 (1938) 309-319.
- 525 [36] B.C. Lippens, J. De Boer, Studies on pore systems in catalysts: V. The t method, *J. Catal.* 4
526 (1965) 319-323.
- 527 [37] M. Thommes, K. Kaneko, A.V. Neimark, J.P. Olivier, F. Rodriguez-Reinoso, J. Rouquerol,
528 K.S. Sing, Physisorption of gases, with special reference to the evaluation of surface area and
529 pore size distribution (IUPAC Technical Report), *Pure Appl. Chem.* 87 (2015) 1051-1069.
- 530 [38] Y.H. Yoon, J.H. Nelson, Application of gas adsorption kinetics I. A theoretical model for
531 respirator cartridge service life, *Am. Ind. Hyg. Assoc. J.* 45 (1984) 509-516.
- 532 [39] G. Zhuang, Z. Zhang, J. Sun, L. Liao, The structure and rheology of organo-montmorillonite
533 in oil-based system aged under different temperature, *Appl. Clay Sci.* 124 (2016) 21-30.
- 534 [40] J. Zhu, W. Shen, Y. Ma, L. Ma, Q. Zhou, P. Yuan, D. Liu, H. He, The influence of alkyl chain
535 length on surfactant distribution within organo-montmorillonites and their thermal stability, *J.*
536 *Therm. Anal. Calorim.* 109 (2012) 301-309.
- 537 [41] Y. Wang, P. Zhang, K. Wen, X. Su, J. Zhu, H. He, A new insight into the compositional and
538 structural control of porous clay heterostructures from the perspective of NMR and TEM,
539 *Micropor. Mesopor. Mat.* 224 (2016) 285-293.
- 540 [42] A. Palazov, Benzene adsorption and its interaction with carbon monoxide on
541 alumina-supported platinum—An infrared spectroscopic study, *J. Catal.* 30 (1973) 13-20.
- 542 [43] A. De Mallmann, D. Barthomeuf, Change in benzene adsorption with acidobasicity of (Cs,
543 Na) X zeolites studied by ir spectroscopy, *Zeolites* 8 (1988) 292-301.
- 544 [44] Y. Du, H. Wang, S. Chen, Study on alkylation of benzene with ethylene over β -zeolite catalyst

- 545 to ethylbenzene by in situ IR, *J. Mol. Catal. A-Chem.* 179 (2002) 253-261.
- 546 [45] W. Wang, X. Ma, S. Grimes, H. Cai, M. Zhang, Study on the absorbability, regeneration
547 characteristics and thermal stability of ionic liquids for VOCs removal, *Chem. Eng. J.* 328
548 (2017) 353-359.
- 549 [46] L. Deng, P. Du, W. Yu, P. Yuan, F. Annabi-Bergaya, D. Liu, J. Zhou, Novel hierarchically
550 porous allophane/diatomite nanocomposite for benzene adsorption, *Appl. Clay Sci.* 168 (2019)
551 155-163.
- 552 [47] E. Sabio, E. González, J. González, C. González-García, A. Ramiro, J. Ganan, Thermal
553 regeneration of activated carbon saturated with p-nitrophenol, *Carbon* 42 (2004) 2285-2293.
- 554 [48] K.S. Hwang, D.K. Choi, S.Y. Gong, S.Y. Cho, Adsorption and thermal regeneration of
555 methylene chloride vapor on an activated carbon bed, *Chem. Eng. Sci.* 52 (1997) 1111-1123.
- 556

Table 1 Total carbon (f_C) and nitrogen (f_N) content of Na-Mt and TMA-Mtx samples.

Samples	f_C (by mass, %)	Δf_C	f_N (by mass, %)	Δf_N
Na-Mt	0.074	0.000	0.044	0.000
TMA-Mt _{0.25}	1.720	1.646	0.380	0.336
TMA-Mt _{0.5}	2.700	2.626	0.720	0.676
TMA-Mt _{1.0}	4.270	4.196	1.100	1.056
TMA-Mt _{1.5}	4.600	4.526	1.160	1.116
TMA-Mt _{2.0}	4.750	4.676	1.240	1.196

Note: $\Delta f_C = f_C$ (TMA-Mt) - f_C (Na-Mt), $\Delta f_N = f_N$ (TMA-Mt) - f_N (Na-Mt).

Table 2 Porous parameters of Na-Mt and TMA-Mtx samples

Samples	S_{BET} (m ² /g)	V_{total} (cm ³ /g)	S_{micro}^a (m ² /g)	V_{micro}^a (cm ³ /g)
Na-Mt	55.9	0.092	3.3	0.001
TMA-Mt _{0.25}	69.6	0.094	19.0	0.007
TMA-Mt _{0.5}	147.9	0.131	59.9	0.023
TMA-Mt _{1.0}	154.7	0.139	61.8	0.024
TMA-Mt _{1.5}	173.5	0.150	65.0	0.025
TMA-Mt _{2.0}	160.2	0.134	55.9	0.021

^a Microporous surface area and volume were calculated by the t -plot method

Table 3 Dynamic adsorption capacity (q) and Yoon and Nelson equation parameters for benzene adsorption of Na-Mt and TMA-Mtx samples.

Samples	q (mg/g)	k	τ (min)	R^2
Na-Mt	87.1	0.263	30.0	0.990
TMA-Mt _{0.25}	184.3	0.113	59.1	0.972
TMA-Mt _{0.5}	220.9	0.094	72.3	0.982
TMA-Mt _{1.0}	380.8	0.083	126.6	0.986
TMA-Mt _{1.5}	425.3	0.059	140.6	0.985
TMA-Mt _{2.0}	419.0	0.058	138.9	0.987

Table 4 Dynamic adsorption capacity (q) and Yoon and Nelson equation parameters for various cycles of TMA-Mt_{1.5}.

Cycles	q (mg/g)	k	τ (min)	R^2	Efficiency (%)
First	425.3	0.059	140.6	0.985	–
Second	414.8	0.060	137.5	0.987	97.5%
Third	403.7	0.065	134.3	0.988	94.9%
Fourth	385.2	0.082	128.4	0.989	90.6%

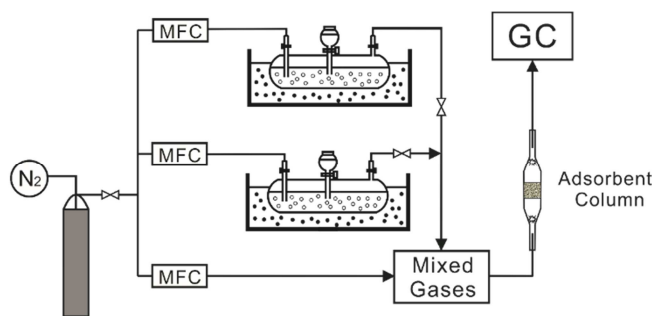


Fig. 1 Schematic diagram of experimental set-up.

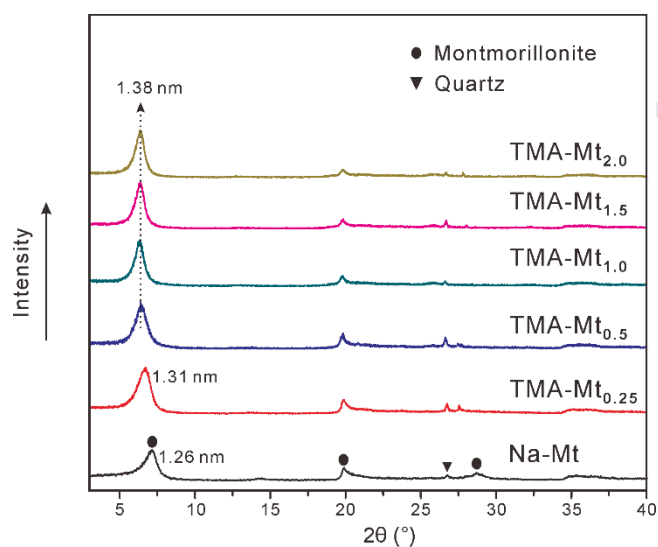


Fig. 2 XRD patterns of Na-Mt and TMA-Mtx samples.

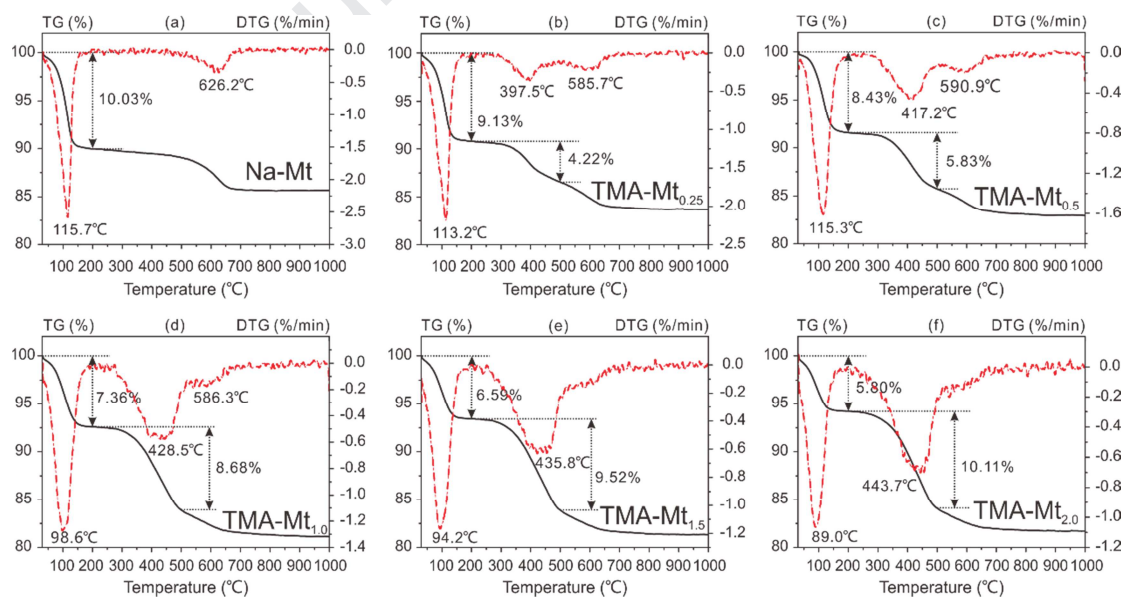


Fig. 3 TG and DTG curves of (a) Na-Mt, (b) TMA-Mt_{0.25}, (c) TMA-Mt_{0.5}, (d) TMA-Mt_{1.0}, (e)

TMA-Mt_{1.5}, and (f) TMA-Mt_{2.0}.

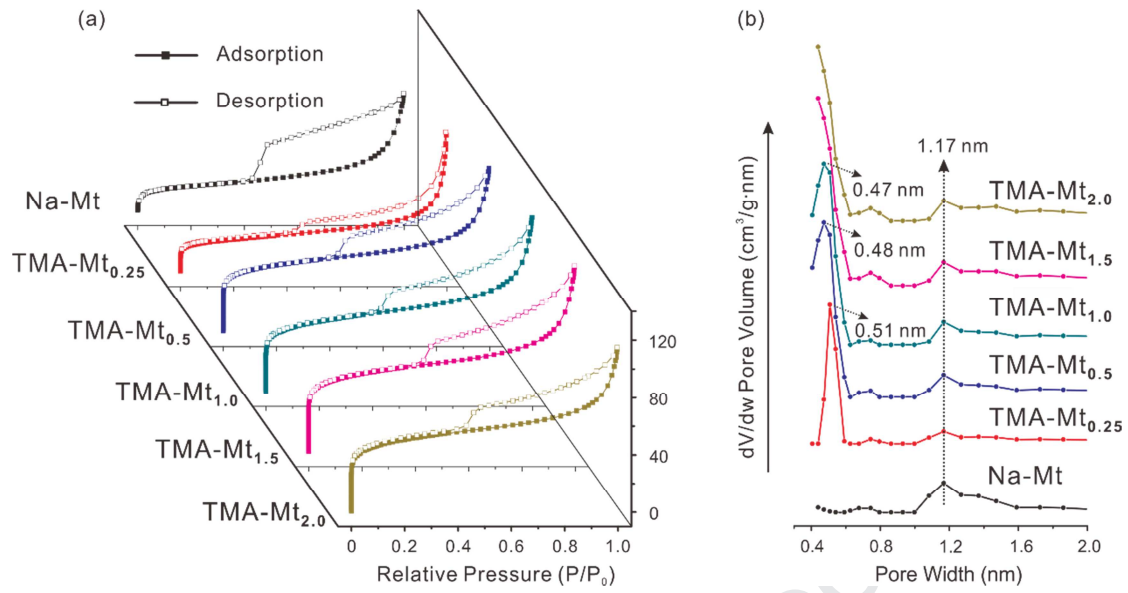


Fig. 4 Ar adsorption-desorption isotherms (a) and NLDFT pore size distribution (PSD) curves (b)

of Na-Mt and TMA-Mtx samples.

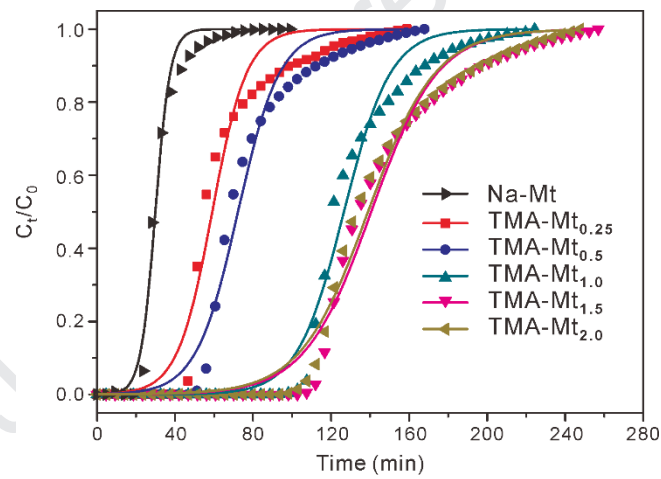


Fig. 5 Breakthrough curves of Na-Mt and TMA-Mtx samples.

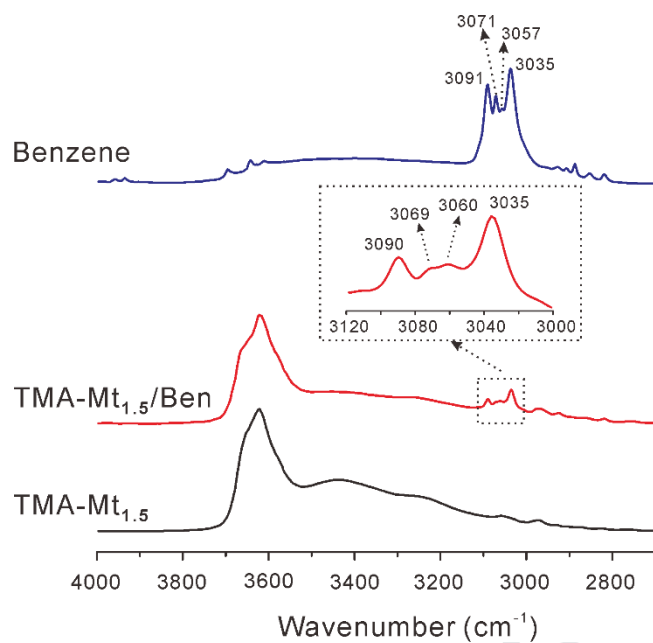


Fig. 6 DRIFT spectra of benzene, TMA-Mt_{1.5}, and TMA-Mt_{1.5}/Ben.

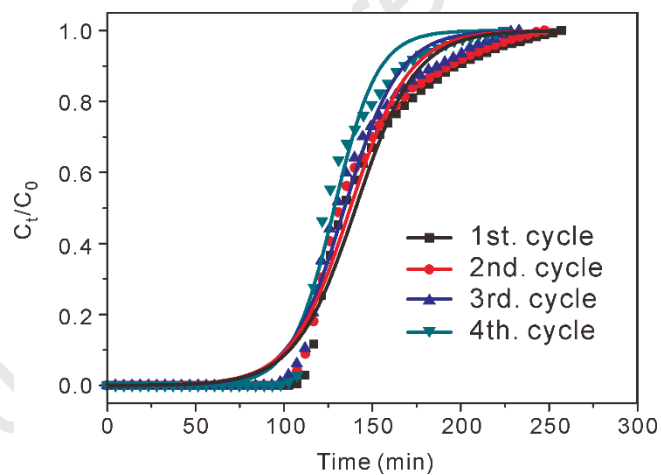


Fig. 7 Benzene adsorption breakthrough curves of TMA-Mt_{1.5} cycled for four times.

Highlights:

- 1) Tetramethylammonium exchanged montmorillonite (TMA-Mt) was prepared.
- 2) The dynamic benzene adsorption performance of TMA-Mt was investigated.
- 3) TMA-Mt possessed an interlayer microporous structure.
- 4) TMA-Mt exhibited excellent dynamic benzene adsorption performance.
- 5) Remarkable regenerability was demonstrated on TMA-Mt for benzene adsorption.

Credit Author Statement

Liangliang Deng: Conceptualization, Investigation, Writing - Original Draft;

Yaqi Liu: Investigation;

Guanzheng Zhuang: Writing-Reviewing and Editing;

Peng Yuan: Supervision;

Dong Liu: Resources;

Hongling Bu: Resources;

Hongzhe Song: Resources;

Li Li: Resources;

Declaration of interests

We declare that we have no known competing financial interests or personal relationships that could have appeared to influence the work reported in this paper.

Journal Pre-proof